Biomaterials Science



PAPER

View Article Online



Cite this: *Biomater. Sci.*, 2025, **13**, 1554

Enhanced combination therapy through tumor microenvironment-activated cellular uptake and ROS-sensitive drug release using a dual-sensitive nanogel†

Jianming Yuan,‡ Qinfeng Chen,‡ Mingxiang Zuo,‡ Xiaoxia Li,‡ ChiYi Ou, Qinghua Chen, Dongsheng Yu, Haowen Li, Chenhui Hao, Jing Yang, Shuang Liu and Du Cheng **

Although the co-delivery of chemotherapeutic and photodynamic agents has been studied for years, developing a simple and efficient nanoplatform for high co-delivery efficiency remains a challenge for clinical applications. In this study, we prepared a reactive oxygen species (ROS) and pH dual-sensitive nanogel for the co-encapsulation of doxorubicin (DOX) and indocyanine green (ICG)-conjugated bovine serum albumin (BSA) via a simple inverse miniemulsion polymerization process. This was followed by modification with pegylated cell-penetrating peptides (CPPs) containing citraconic anhydride (CDM) linkers, which are sensitive to weakly acidic microenvironments (pH 6.5). Pegylation endowed the nanogel with extended blood circulation, while the de-shielding of polyethylene glycol (PEG) exposed the CPPs, significantly enhancing cellular uptake. Upon near-infrared (NIR) irradiation, ROS generated by ICG not only killed tumor cells but also triggered the release of DOX through nanogel disintegration. Serial experiments verified the nanogel's high co-delivery efficiency, tumor tissue matrix microenvironment-triggered cellular uptake, controlled drug release, and synergistic antitumor effects. Therefore, this dual-sensitive nanogel, prepared via inverse miniemulsion polymerization, offers a facile approach to improving co-delivery efficiency for combination therapy.

Received 16th October 2024, Accepted 11th February 2025 DOI: 10.1039/d4bm01377h

rsc.li/biomaterials-science

1. Introduction

Doxorubicin (DOX), a first-line clinical antitumor drug, plays a crucial role in antitumor therapy. However, its inherent limitations—such as drug resistance, adverse effects, and relatively low therapeutic efficacy—hinder its overall clinical outcomes.¹ To enhance the effectiveness of DOX-based therapies, several approaches have been developed in combination with DOX. For instance, small molecular drugs (e.g., arsenite, elacridar, and indocyanine green (ICG)) and small interfering RNA (siRNA) molecules have been co-loaded with DOX using polymeric micelles and vesicles.^{2–10} Additionally, nanogold particles have been employed to encapsulate DOX for combined photothermal therapy (PTT),^{10–13} while photodynamic therapy (PDT) has been combined with DOX to enhance its antitumor

Key Laboratory for Polymeric Composite & Functional Materials of Ministry of Education, School of Materials Science and Engineering, Sun Yat-sen University, Guangzhou 510275, PR China. E-mail: chengdu@mail.sysu.edu.cn

†Electronic supplementary information (ESI) available. See DOI: https://doi.org/10.1039/d4bm01377h

‡These authors contributed equally.

effect using photosensitizers such as ICG, chlorin e6 (Ce6), and hematoporphyrin. ^{7,12,14-20} Despite these advances, several challenges remain: (i) the co-encapsulation process is often time-consuming and labor-intensive, limiting its clinical application; (ii) the limited availability and high cost of targeting ligands restrict their use in tumor-targeted delivery, and modifying these ligands may compromise blood circulation performance; and (iii) uncontrolled tumor cell-specific cellular uptake and drug release can cause side effects in normal tissues. Therefore, alternative strategies are required to improve combination therapies in terms of preparation, targeted delivery, and controlled drug release.

Amphiphilic copolymers play important roles in the codelivery of two or more drugs due to their ability to self-assemble. The copolymers consist of two or more blocks: hydrophobic blocks (*e.g.*, polycaprolactone (PCL), polyphenylalanine, and poly(2-(diisopropylamino)ethyl methacrylate)) that assemble with DOX into a hydrophobic core; cationic hydrophilic blocks (*e.g.*, polyetherimide, poly(aspartic acid-ethylthioketal quaternary amino), and poly(*N*-(2,2'-dithiobis(ethylamine)) aspartamide)) that complexes with siRNA to form an interlayer; and an outer hydrophilic shielding layer composed

of polyethylene glycol (PEG). 2,3,21-28 These amphiphilic copolymers have been used to prepare vesicles to co-deliver DOX and other small molecular drugs, as well as nanogold, using encapsulation and conjugation methods.^{7,11,12,22} Recently, nanogels prepared via inverse emulsion polymerization have garnered increased attention due to their ease of preparation, low cost, high encapsulation efficiency, and excellent stability.²⁹⁻³⁸ As such, DOX encapsulation through inverse emulsion polymerization represents an effective strategy for enhancing synergistic effects of DOX-based combination therapies. Betaine-based nanogels have garnered increasing attention due to several advantages: (i) the superior hydrophilicity and antifouling properties of betaine confer high stability and prolonged blood circulation time to the nanogels;³⁹ (ii) the low immunogenicity of natural betaine imparts higher biocompatibility to the nanogels compared to polyethylene glycol (PEG); 40-42 (iii) the zwitterionic nature of betaine prevents macrophage uptake, 43 thereby enhancing tumor accumulation.

PDT offers a unique advantage in spatially controlled, tumor-specific combination therapy.²¹ For example, the copolymer nitrilotriacetic acid (NTA)-terminated-poly(ethylene glycol)-b-polycaprolactone was synthesized and self-assembled with the photosensitizer Ce6 into nanoparticles, which were employed to bind Cas9/sgRNA through interaction with the NTA moiety. This approach enabled tumor-specific gene editing, triggered by Ce6-induced PDT. The co-delivery of siRNA and Ce6 using a ROS-sensitive copolymer facilitated PDT-triggered siRNA release, enabling spatially controlled siRNA therapy. 44 The photosensitizer ICG has shown superior PDT effects owing to its high conversion efficiency and long excitation wavelength. In view of this, combining ICG-based PDT with DOX is a feasible approach to achieve tumor-specific targeting and controlled release of DOX.

Despite decades of development, the delivery of nanomedicines remains challenging, particularly in balancing long blood circulation time with efficient, specific cellular uptake. Although the neutral or protein-repellent surface of nanomedicines helps prevent clearance during blood circulation, it may hinder cellular uptake. To enhance specific cellular uptake, antibodies are often introduced as targeting ligands on the surface of nanomedicines. However, while this approach substantially promotes cellular uptake, it tends to reduce blood circulation time due to the high molecular weight of antibodies and non-specific interactions with serum proteins. These conflicting requirements—prolonged blood circulation and highly efficient, specific cellular uptake-present considerable challenges in improving the overall delivery efficiency of nanocarriers. The emergence of the charge-reversal strategy provides an alternative approach to overcome this barrier. Nanoparticles containing citraconic anhydride (CDM) structures and substrate peptides of matrix metalloproteinase 2 (MMP2) showed nearly neutral zeta potential during blood circulation, but generated a highly positive zeta potential in response to the weakly acidic condition and MMP2 enzymes in the tumor tissue matrix, 31,45,46 owing to cleavage-generated primary amines. Additionally, low pH (e.g., hydrazone, acetal,

and imine) and/or ROS (e.g., thioketal, diselenide bond, and proline)-sensitive bonds were incorporated to control drug release through bond cleavage. 47-49 Moreover, sensitive moieties such as 2-diisopropylamino, 2-dimethylamino, and imidazole for low pH, and methylsulfanyl, arylboronate, and thiazolidinone for ROS, were introduced into nanomedicines to enable controlled drug release. 50-52 ROS-sensitive structures have been introduced into nanocarriers to enable ROS-triggered drug release, facilitating combination therapy involving PDT agents and other drugs. 21,31 However, the combined strategy of low pH-induced charge reversal and ROS-triggered drug release through sequential actions remains largely unexplored as a synergistic approach to enhancing the antitumor efficacy of nanomedicine. Thus, incorporating CDM and ROS-sensitive structures into nanogels may significantly enhance co-delivery efficiency of DOX and ICG, thus achieving PDT-triggered drug release.

In this study, we developed a pH and ROS dual-sensitive betaine-based nanogel to co-encapsulate DOX and ICG-conjugated BSA (ICG-BSA) through inverse emulsion polymerization (Fig. 1), involving the use of a carboxybetaine (CBAA) monomer and ROS-sensitive crosslinker. The nanogel was further modified with pH-activated peptide polymers. The PEG shielding and zwitterionic CBAA endowed the nanogel with long blood circulation time. Upon reaching the tumor tissue, the weakly acidic microenvironment triggered the cleavage of CDM, thereby unmasking the CPP and enhancing cellular internalization. NIR irradiation spatially induced ROS generation within tumor tissue and promoted DOX release due to the nanogel disintegration from the cleavage of crosslinkers. This strategy provides a facile approach to enhancing the efficacy of combination therapy through spatially controlled synergistic drug effects.

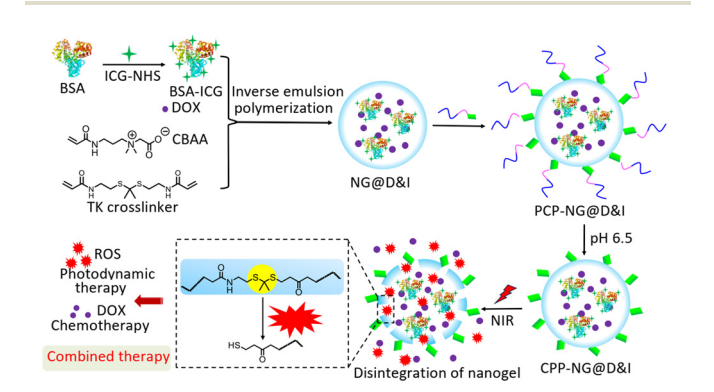


Fig. 1 Schematic of the preparation and antitumor mechanism of nanogels loading DOX and ICG. The inverse miniemulsion polymerization-based nanogel preparation provides a facile nanoplatform for coencapsulating DOX and ICG, enabling a combination of PDT and chemotherapy. PEG shielding, exposure of CPPs in tumor tissue, and ROS-induced cleavage of the crosslinker endows the nanogel with prolonged circulation time enhanced tumor-specific cellular internalization, and controlled drug release, ultimately achieving improved synergistic antitumor efficacy.

2. Materials and methods

2.1 Materials

Paper

Chemical and biological reagents are detailed in the ESI.†

2.2 Syntheses of carboxybetaine monomer CBAA, thioketal crosslinker TK-CL, and polymer PEG-CDM

The syntheses of CBAA, TK-CL, and PEG-CDM are described in detail in the ESI. $\!\!\!\!^{\dagger}$

2.3 Preparation of nanogels loaded with DOX and ICG-BSA

The preparation of ICG-BSA is detailed in the ESI.† The DOX and ICG-BSA-loaded nanogel was prepared according to the following method: in a 50 mL serum bottle, 0.50 g of sodium bis(2-ethylhexyl) sulfosuccinate (AOT) and 1.00 g of polyethylene glycol lauryl ether (Brij 30) were mixed with 20 mL of *n*-hexane. The mixture was vigorously stirred until all reagents were completely dissolved, followed by purging with nitrogen gas for 10 min. For aqueous phase, 5 mg of ICG-BSA and 0.16 mg of DOX were dissolved in 290 µL of PBS buffer solution (pH 8.0). Then, 200 mg of CBAA monomer, 20 mg of TK-CL, and 110 µL of ammonium bicarbonate solution (2 µg μL⁻¹) were added and dissolved into the DOX/ICG-BSA solution. After bubbling with nitrogen for 5 min, the aqueous solution was slowly added dropwise to the organic continuous phase. A stable microemulsion was prepared after ultrasonic treatment. Subsequently, 10 µL of ammonium persulfate (APS) solution (20% (w/v)) was added to the emulsion. Five minutes later, polymerization was initiated by adding 8 µL of tetramethylethylenediamine (TEMED), followed by rapid stirring at 4 °C. After 1 h of reaction, 200 μL of DOX solution (10 mg mL⁻¹) was introduced, and the reaction continued for an additional 2 h. After removing the organic solvent through vacuum distillation via a rotary evaporator, the nanogels were precipitated. The resulting precipitate was washed three times with cold acetone and then dried under vacuum for 30 min. The resulting precipitate was resuspended in PBS buffer solution (pH 7.4), and the suspension was centrifuged to remove insoluble materials. The clear liquid was purified using an ultrafiltration tube with a molecular weight cut-off (MWCO) of 100 kDa to remove free ICG-BSA and DOX. The resulting nanogel containing DOX and ICG-BSA was referred NG@D&I.

2.4 Surface modification with pH-sensitive shielding layer

First, 1 mg of cell-penetrating peptide (CPP) terminated with sulfhydryl group. 3-Mercaptopropionic acid was dissolved in purified water. Then, 1.8 mg of 1-(3-dimethylaminopropyl)-3-ethylcarbodiimide hydrochloride (EDCI) and 1.1 mg of *N*-hydroxysuccinimide (NHS) were added to the CPP solution. The mixture was stirred at room temperature for 6 h, followed by continuously stirring at 4 °C for an additional 12 h. Afterwards, the solution was dialyzed against PBS (pH 7.4) using an ultrafiltration tube (MWCO: 1 kDa) to obtain CPP-SH. Secondly, the modification on the surface of NG@D&I with CPP was conducted *via* the reaction between the sulfhydryl group on CPP and the residual carbon–carbon double bond on

the surface of nanogel. Briefly, the nanogel and CPP-SH were mixed in PBS solution (pH 7.4), and 100 µg of sodium bisulfite and 100 µg of ammonium persulfate were introduced into the mixture. After reacting at 4 °C for 12 h, the reaction solution was concentrated and purified three times using an ultrafiltration tube (MWCO: 100 kDa) to obtain the CPP-modified nanogel, referred to as CPP-NG@D&I. Finally, nanogels coated with pH-sensitive shielding layer were prepared through the reaction between acid anhydride of PEG-CDM-CPP and the surface of nanogel. In brief, 50 mg of PEG2k-CDM and 36 mg of CPP peptide were dissolved in 10 mL of DMF and stirred for 12 h. The reaction solution was precipitated with ether, and the precipitate was collected through centrifugation. The resulting precipitate was dried under vacuum to obtain 72.5 mg of white powder (PEG_{2k}-CDM-CPP), denoted as PCP. Next, 230 µg of PCP, 12 µg of mercaptopropionic acid, 35 µg of EDCI, and 22 μg of NHS were added to DMSO (3 mL). The reaction was performed for 12 h. Afterwards, 50 µg of sodium bisulfite, 50 µg of ammonium persulfate, and a predetermined amount of NG@D&I were added and further reacted at 4 °C for 12 h. The resulting solution was filtered through ultrafiltration to get the final product, PEG-CDM-CPP modified NG@D&I, referred to as PCP-NG@D&I.

2.5 Loading content and efficiency

The loading efficiency (LE) and loading content (LC) of DOX and ICG in PCP-NG@D&I were determined using ultraviolet (UV) absorption analysis at 488 nm and 780 nm, respectively, with a UV-Vis spectrophotometer (UV-2000, Shanghai, China). In brief, a predetermined amount of lyophilized PCP-NG@D&I powder was dissolved in a certain volume of PBS buffer solution. The absorbance of DOX was measured, and the mass of DOX in the PCP-NG@D&I powder was calculated using the previously established calibration curve. The calibration curve of DOX concentrations versus absorbance values at 488 nm was created using known concentrations of DOX solution. The LE and LC of DOX in the PCP-NG@D&I were calculated according to the following formulas: LE = (mass of DOX loaded in PCP-NG@D&I nanogel/mass of DOX in feed) × 100%, LC = (mass of DOX loaded in PCP-NG@D&I nanogel/mass of lyophilized PCP-NG@D&I nanogel) × 100%. The method for determining LE and LC of ICG is identical to that for DOX, with absorbance measured at 780 nm.

2.6 DOX release

To evaluate pH- and ROS-sensitive release capacity of the nanogel, 2 mL of DOX-encapsulated nanogel solution was adjusted to specific pH values using different buffer solutions, with or without 10 mM H₂O₂ (*i.e.*, pH 6.5, pH 7.4, pH 6.5 with 10 mM H₂O₂, and pH 7.4 with 10 mM H₂O₂). The solutions were transferred into dialysis bags with a MWCO of 14 kDa. These bags were submerged in 40 mL of corresponding buffer and placed in an incubate shaker with gentle shaking (75 rpm) at 37 °C to mimic *in vivo* conditions. At predetermined time points, 3 mL of buffer was withdrawn from outside the dialysis bag to measure the amount of DOX using UV/Vis analysis, and

Biomaterials Science

3 mL of fresh solution was added to replenish the volume. The amount of DOX was calculated based on the absorbance values at 480 nm against concentration. The cumulative DOX release amount was presented as total amount of released DOX during incubation.

2.7 Cellular uptake

Human breast tumor cells MDA-MB-231 cells were plated in culture dishes with glass bottoms at a cell density of 1×10^3 cells per well and cultured overnight under the condition of 5% CO₂ at 37 °C. After replenishing cells with fresh culture medium, different nanogels were added at a concentration of 100 ng mL⁻¹ at pH values of 7.4 and 6.5, respectively. Following a 2 h-incubation, the cells were washed three times with PBS solution. The Hoechst 33342 (5 μg mL⁻¹) was used to stain the nuclei. After washing the cells three more times with PBS buffer solution, the cells were analyzed using confocal laser scanning microscope (CLSM). To quantitatively evaluate cellular uptake efficiency, cells treated with different nanogels were digested with 0.25% of pancreatin and washed three times with PBS solution. The resulting cells were collected through centrifugation and resuspended in PBS solution. The FITC fluorescence dye was conjugated to BSA instead of ICG fluorescence dye for preparing nanogel PCP-NG@D&F. The percentages of DOX- and FITC-positive cells were analyzed using flow cytometry (Gallios, Beckman). Moreover, we added different endocytosis inhibitors (i.e., dynasore, amiloride, β-cyclodextrin, NaN₃, chlorpromazine, and heparin) of cellular endocytosis into culture medium for exploring the cellular uptake pathway of PCP-NG@D&I. After pre-incubation for 2 h with culture medium containing different inhibitors, cells were treated with PCP-NG@D&I and subjected to NIR irradiation under the condition of pH 6.5. The NIR irradiation (808 nm, 1 W cm⁻²) was conducted for 5 min. After irradiation, the cells were co-incubated with the nanogels for another 2 h, washed three times with PBS solution, digested with pancreatin enzymes, and collected through centrifugation. The resulting cellular precipitate was lysed with sodium dodecyl sulfate (SDS), and the lysate was subjected to UV-absorption analysis at 488 nm to determine cellular content of DOX.

2.8 ROS generation and intracellular distribution of DOX

To investigate the ROS generation capacity of different nanogels under NIR irradiation, 1×10^5 cells were seeded in each well of 24-well culture plate and cultured overnight. After incubating with nanogels for 4 h, the ROS probe 2',7'-dichlorodihydrofluorescein diacetate (DCFH-DA) was added to the culture medium at a concentration of 10 µM. Following a 30 min coincubation, the medium was replaced with fresh medium (pH 6.5), and the cells were subjected to NIR irradiation with a wavelength of 808 nm for 5 min at a power of 1 W cm⁻². The oxidazed DCFH-DA (green fluorescence) by ROS and the intracellular distribution of DOX (red fluorescence) were recorded using CLSM. These cells were then digested with pancreatin (0.25%), collected through centrifugation, and analyzed using flow cytometry.

2.9 Cell viability

The cytotoxicity of nanogels to MDA-MB-231 cells was evaluated using 3-(4,5)-dimethylthiahiazo(-z-y1)-3,5-di-phenytetrazoliumromide (MTT) assay. MDA-MB-231 cells were seeded at a density of 1×10^3 cells per well to 96-well plate and cultured overnight. After cells were replenished with fresh medium, tumor cells were treated with nanogels for 24 h at different concentrations: 1.0 to 20 μg mL⁻¹ for ICG and 0.1 to 2.0 μg mL⁻¹ for DOX, respectively. NIR irradiation was performed if necessary. After treatment, 10 μL of MTT solution (5 mg mL⁻¹) was added into each well and incubated for 4 h. Then, 90 µL of DMSO was added to dissolve the resulting blue MTT-formazan crystals. Absorbance at 570 nm was recorded using a microplate reader (Tecan Infinite F200, Crailsheim, Germany). Cell viability was calculated according to the following formula: Cell viability = (absorbance of sample/absorbance of control) \times 100%. Based on the drug concentration-cell viability curve, the drug concentration resulting in 50% of cell viability (IC50) was determined.

2.10 Animal model

MDA-MB-231 tumor-bearing animal model was established using six-weeks-old female BALB/c nude mice, each weighing 15-20 g, purchased from the Guangdong Medical Laboratory Animal Center (Guangzhou, China). All animal procedures were performed in accordance with the Guidelines for Care and Use of Laboratory Animals of Sun Yat-sen University and approved by the Animal Ethics Committee of Sun Yat-sen University. A total of 1×10^6 tumor cells were implanted subcutaneously into the left flank of each nude mouse.

2.11 In vivo biodistribution

In vivo biodistribution studies of PCP-NG@D&I and PC-NG@D&I were conducted using the FX Pro in vivo fluorescence imaging system from Carestream Health Corporation (New Haven, CT, USA). Once the tumor volume reached approximately 100 mm³, the nanogels were administered intravenously at a dose of 5 mg ICG per kg body weight. Fluorescence imaging of ICG-encapsulated nanogel was performed at predetermined time points. At 36 h after nanogel injection, animals were sacrificed, and the tumors and major organs from animals in different groups were excised for ex vivo fluorescence imaging analysis.

2.12 In vivo antitumor effect

When the tumor volume reached 50 mm³, the tumor-bearing animals were randomly divided into seven groups, each receiving different nanoparticles: PBS control, blank nanogel without Dox and ICG (PCP-NG), DOX alone (PCP-NG@D without NIR irradiation), ICG alone (PCP-NG@I), pH-nonsensitive combination therapy (PP-NG@D&I), combination therapy without CPP peptides (PC@D&I), combination therapy (PCP-NG@D&I). Once the tumor volume reached approximately 100 mm³, the nanogels were administered intravenously at a dose of 5 mg ICG per kg body weight and 2 mg

Paper

DOX per kg body weight every other day for 19 d following the first injection. At predetermined time points, tumor volumes were measured using the formula: $V = L \times W^2 \times 1/2$ (where V indicates volume, L indicates length, and W indicates width of the tumor). After 24 d post-first injection, the animals were sacrificed, and the tumor tissues were excised, weighed, and photographed. Tumor tissue sections were deparaffinized and hydrated for histopathological analysis including hematoxylin and eosin (H&E) staining and TdT-mediated dUTP Nick-End Labeling (TUNEL) staining.

2.13 Statistical analysis

Data are presented as mean ± standard deviation (SD). Statistical differences were assessed using one-way analysis of variance (ANOVA). Asterisks indicate significance levels: * for p < 0.05, ** for p < 0.01, and *** for p < 0.001.

3. Results and discussion

3.1 Preparation and characterization of molecules, polymer, and nanogels

The CBAA-based monomer, thioketal (TK)-containing crosslinker, and polyethylene glycol modified with citraconic anhydride and CPP peptide (PEG-CDM-Peptide) were synthesized according to the routes outlined in Fig. S1-S4,† and referred to here as CBAA, TK-CL, and PCP, respectively. These materials were characterized using hydrogen nuclear magnetic resonance (¹H-NMR) (Fig. 2). The successful synthesis of CBAA was confirmed by the appearance of characteristic peaks at 3.70 ppm (6H, $-N(CH_3)_2$), 4.30 ppm (2H, $-CH_2-COO^-$), 5.80 ppm (1H, -CH₂=CH-), and 6.10 ppm (2H, -CH₂=CH-) (Fig. 2A). For TK-CL, the characteristic peaks at 1.50 ppm (6H, 5.70 (1H, $-CH_2=CH-),$ $-S-C(CH_3)_2-S-),$ ppm 6.10-6.20 ppm (2H, -C H_2 =CH-) confirmed its structure (Fig. 2B). PEG-CDM showed characteristic peaks at the 2.70 ppm (4H, $-OCO-(CH_2)_2-$) and 1.90-1.95 ppm (3H, $-CH_2 C(CO) = C(CH_3)COO-),$ indicating successful (Fig. 2C). The conjugation of the CPP peptide to PEG-CDM to form the PCP polymer was confirmed by characteristic peaks at the 2.95 ppm (4H, -OCO-(CH₂)₂-), 2.60-2.70 ppm (3H, $-CH_2-C(CO)=C(CH_3)COO-$) and 3.10-3.20 ppm (characteristic H of CPP peptide) (Fig. 2D). The conjugation rate of CPP peptides was calculated to be 53.8% according to the integral area ratio between 2.95 ppm (characteristic H of mPEG_{2k}) and 3.10-3.20 ppm (characteristic H of CPP peptide) in the ¹H-NMR spectrum. Furthermore, the PEG-CDM-CPP polymer exhibited a molecular weight of approximately 3623, as determined by matrix-assisted laser desorption/ionization time of flight mass spectrometry (MALDI-TOF MS) analysis (Fig. S5†). Additionally, a highly hydrophilic form of ICG was prepared through conjugating it to bovine serum albumin (B-ICG). This conjugation enhances ICG encapsulation efficiency and provides higher intracellular stability than free ICG by preventing non-specific binding to proteins and subsequent clearance by macrophage cells.⁵³ After the removal of free ICG, the grafting

percentage of ICG to BSA was determined to be $2.21 \pm 0.11\%$ based on the standard curve of ICG concentrations versus absorbance at 780 nm (Fig. S6A and B†). Moreover, B-ICG demonstrated identical UV/Vis absorption and ROS generation capacity compared to free ICG (Fig. S6†).

The CBAA monomers and TK-CL crosslinkers were used to fabricate nanogels for the encapsulation of DOX and B-ICG through inverse miniemulsion polymerization (Fig. 1). Given that the important roles of surfactant/stabilizer, ratio of oilwater, use of monomer and crosslinker in inverse miniemulsion polymerization, we investigated the size, polydispersity index (PDI), yield, and drug release of nanogels under different conditions (Fig. S7†). First, the mass ratio of sodium bis(2-ethylhexyl) sulfosuccinate (AOT) to polyethylene glycol lauryl ether (Brij 30) (M_{AOT}/M_{Brij}), which were used as surfactant and stabilizer, respectively, achieved the smallest size and lowest PDI value at an M_{AOT}/M_{Brij} of 1/2, while the greater or lower M_{AOT}/M_{Brij} ratio increased both size and PDI (Fig. S7A†). Although a lower volume ratio of PBS to n-hexane (V_{PBS}/V_{hexane}) resulted in a smaller size, the lowest PDI value of approximately 0.13 was observed at a V_{PBS}/V_{hexane} of 3/100 (Fig. S7B†). Notably, in addition to affecting nanogels' size and PDI, the use of monomer and crosslinker also significantly influenced both the nanogel yield and drug release (Fig. S7C and D†). A decrease in the mass of crosslinker (M_{TK-CL}) relative to the mass of monomer (M_{CBAA}) (M_{TK-CL}/M_{CBAA}) led to a reduction in nanogel yield, although the yield remained above 90%. The polymerization yields exceeding 100% may be attributed to the residue of surfactant. The nanogel size and PDI at the M_{TK-CL} $M_{\rm CBAA}$ ratios above 1/10 were similar, while ratios below 1/25 produced significantly greater sizes and PDIs. Additionally, the increased use of crosslinker relative to monomer significantly inhibited DOX release from the nanogel (Fig. S8D†), which can be attributed to the formation of more cross-linked networks. Therefore, the optimized polymerization conditions for nanogel preparation are a 1/2 ratio of M_{AOT}/M_{Brii} , a 3/100 ratio of $V_{\text{PBS}}/V_{\text{hexane}}$, and a 1/10 ratio of $M_{\text{TK-CL}}/M_{\text{CBAA}}$.

After that, CPP peptide alone, PEG-CPP without CDM linker (PP), and PCP polymers were introduced onto the surface of the nanogel to shield against nonspecific protein absorption and facilitate the activation of CPP peptides. The size, zeta potential, and morphology of the different nanogels were analyzed using dynamic scanning laser (DLS) and transmission electronic microscope (TEM) (Fig. 2E and F). The nanogels without PCP modification (NG@D&I) showed a small size of approximately 41 nm and a lower zeta potential of +0.12 mV. Modification with the CPP peptide (CPP-NG@D&I) did not significantly affect the nanoparticle size; however, it remarkably increased zeta potential to approximately +14 mV due to the high content of positive charged amino acids in the CPP peptide (Fig. 2E). In contrast, modification with PCP (PEG-CDM-CPP peptide) increased the size to approximately 52 nm and reduced the zeta potential to +4 mV. Similarly, PP (PEG-CPP peptide) modification produced comparable effects on both nanoparticle size and zeta potential at pH 7.4. Notably, under weakly acidic conditions, the zeta potential of

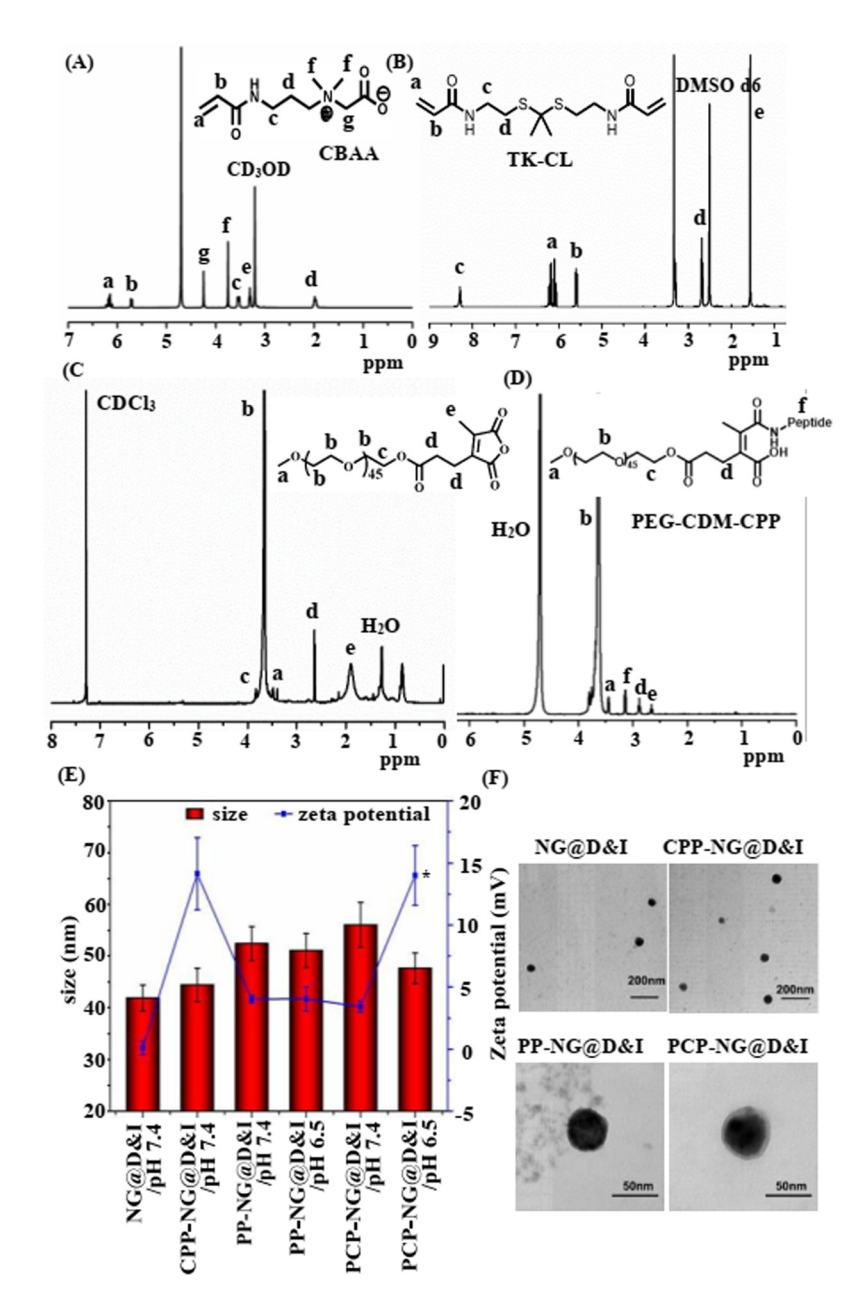


Fig. 2 Characterization of monomer, crosslinker, copolymer, and nanogel. ¹H-NMR analyses of (A) CBAA monomer, (B) TK-CL crosslinker, (C) PEG-CDM polymer and (D) PEG-CDM-CPP polymer. (E) Size and zeta potential of different nanogels. (F) TEM images of different nanogels. Data are presented as mean \pm SD of three replicates. ** indicates p < 0.01 compared to that of PCP-NG@D&I at pH 7.4.

PCP-NG@D&I increased to approximately +14 mV, attributed to the de-shielding of PEG and exposure of the CPP following cleavage of CDM structure. This transformation from PEG deshielding to CPP peptide activation may effectively fulfill the demands in nanomedicines: prolonged blood circulation times, minimized uptake by normal cells, and maximized uptake by tumor cells. The morphology of nanogels showed a spherical shape with a diameter of approximately 50 nm (Fig. 2F), consistent with DLS analysis results. The loading efficiencies of DOX and ICG were 35.2% and 32.1%, respectively, while the loading contents of DOX and ICG were 2.81%

and 2.32% (Fig. S8A†). Additionally, the nanogels showed excellent colloidal stability in the PBS plus 10% serum (Fig. S8B†).

3.2 pH-Sensitive PEG de-shielding and ROS-sensitive DOX release

The pH-sensitive PEG de-shielding capability under the low pH conditions of tumor tissue matrix is essential for achieving tumor cell-specific cellular uptake while minimizing uptake by normal cells. Additionally, the ROS-sensitive DOX release from nanogel promotes rapid attainment of the therapeutic window

for DOX. To assess these properties, we evaluated the PEG deshielding and DOX release capacities of the nanogels under conditions mimicking the weakly acidic and Ce6-generated highly oxidative microenvironments of tumor tissue (Fig. 3A). The DOX release reached a plateau after 24 h of incubation under all conditions. At pH 7.4, less than 10% of the total DOX loaded into the nanogel was released after 24 h (Fig. 3B). This limited release is likely due to the DOX molecules being localized at the interface between the core and the PEG outer layer. In contrast, at pH 6.5, the cumulative release of DOX increased to 17.5%, primarily due to PEG de-shielding, which facilitated enhanced DOX release. Additionally, the improved solubility of DOX at low pH may further facilitate its release. The addition of H2O2 significantly increased DOX release to 55.7%, while the combination of a low pH of 6.5 and H₂O₂ further boosted DOX release to 82.5% after 24 h of incubation.

A similar release profile for ICG was observed under the different conditions (Fig. 3B). Furthermore, we evaluated the DOX release from PCP-NG@D&I under NIR irradiation (Fig. 3C). NIR irradiation significantly enhanced DOX release, increasing the cumulative release by 10-20% per cycle during the 35 min incubation, which is attributed to the cleavage of TK bonds induced by ROS generated from NIR irradiation. At pH 7.4, the nanogels exhibited a smooth surface, whereas at pH 6.5, a rougher surface was observed due to the detachment of the PEG layer induced by CDM cleavage (Fig. 3D). Incubation with H₂O₂ caused the nanogels to disassemble due to the cleavage of the TK-CL crosslinker, and the combination of pH 6.5 and H₂O₂ further enhanced the disassembly of the nanogels. These results demonstrate that the nanogels can effectively detach the PEG layer and synergistically enhance DOX release in response to the conditions of pH 6.5 and ROS.

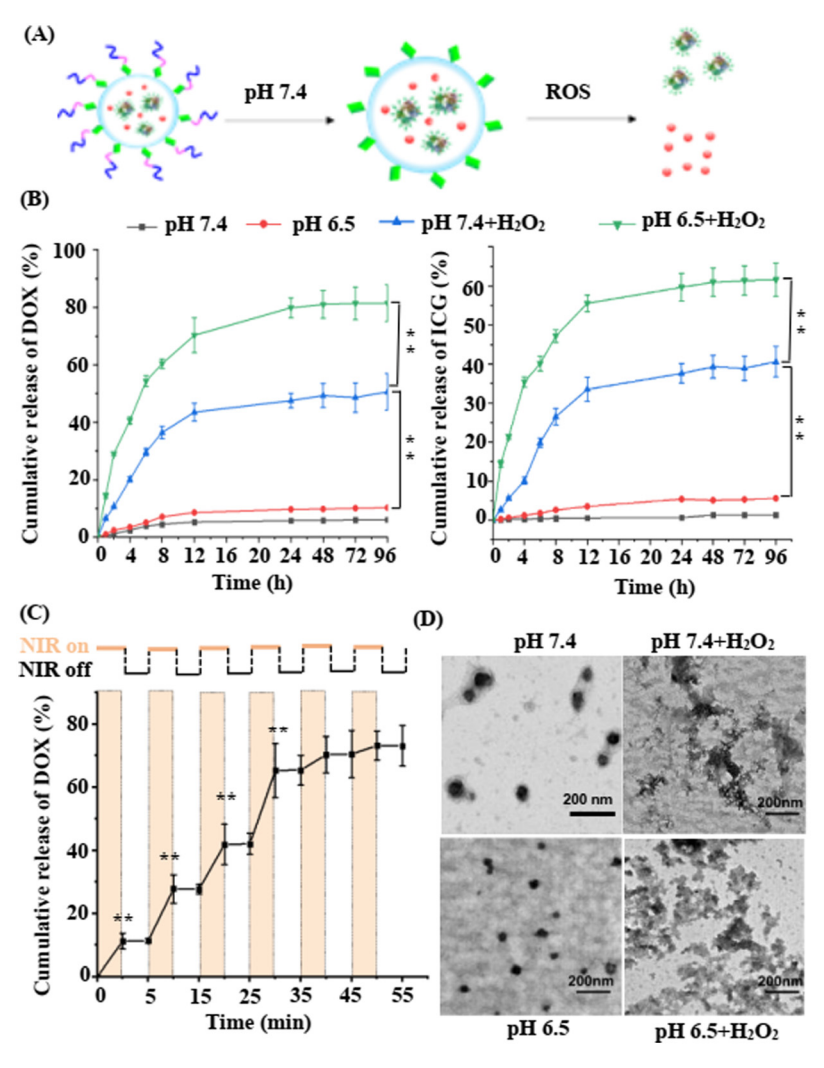


Fig. 3 pH-Sensitive PEG de-shielding and ROS-sensitive DOX release. (A) Schematic illustration of the pH-sensitive PEG de-shielding and ROS-sensitive drug release process. (B) Cumulative releases of DOX and B-ICG under different conditions. *p < 0.05 and **p < 0.01. (C) Cumulative release of DOX under NIR exposure. **p < 0.01 compared to data at previous time point in panel (C). (D) TEM images of PCP-NG@D&I under different conditions. Data are presented as mean \pm SD of three replicates.

3.3 Cellular uptake and intracellular distribution

To investigate the cellular uptake and intracellular distribution of DOX and ICG, we used FITC dyes in place of ICG to conjugate with BSA and visualized tumor cells using confocal laser scanning microscope (CLSM) (Fig. 4). Nanogels modified with CPP peptides alone (CPP-NG@D&F) showed stronger fluorescence signals for both FITC (green) and DOX (red) compared to non-modified nanogels (NG@D&F) (Fig. 4A). Following NIR irradiation, the percentage of DOX fluorescence-positive cells in the PCP-NG@D&F group was approximately 1.7 times higher than in the NG@D&F group (Fig. 4B), indicating enhanced cellular uptake due to PCP modification. Next, we examined the effect of a weakly acidic microenvironment on the uptake of PCP-NG@D&F. At pH 7.4, cells incubated with PCP-NG@D&F exhibited fluorescence signal intensities comparable to those incubated with NG@D&F. However, under pH 6.5, both FITC and DOX fluorescence intensities significantly increased (Fig. 4C). The percentage of dual-positive for FITC and DOX fluorescence at pH 6.5 was approximately 1.6 times higher than at pH 7.4, as measured by flow cytometry (Fig. 4D). These findings indicate that the detachment of the PEG shielding layer in response to the weakly acidic microenvironment (pH 6.5) effectively exposes CPP peptides, thereby enhancing cellular uptake of PCP-NG@D&F. Furthermore, we explored the potential mechanism behind the cellular uptake of PCP-NG@D&I by assessing intracellular DOX content in the presence of different inhibitors (Fig. 4E). Dynasore, an inhibitor of dynamin II-dependent endocytosis, did not affect nanogel uptake at pH 6.5. In contrast, inhibitors of clathrinmediated micropinocytosis (amiloride) and caveolin-mediated endocytosis (β-cyclodextrin) only slightly reduced intracellular DOX levels. Inhibitors of ATP synthesis (NaN3 and 4 °C incubation) reduced the intracellular DOX content by 32%, while inhibitors of clathrin-mediated endocytosis (chlorpromazine, CPZ) and competitive inhibitor of heparan sulfate receptor on the cell surface (heparin) reduced intracellular DOX content by 44% and 68%, respectively. These results indicate that PCP-NG@D&I nanogels are internalized via ATP-dependent and multiple endocytic pathways. Considering that free DOX molecules bind to DNA and localize within nucleus, we evaluated the ROS-sensitive DOX release capacity of PCP-NG@D&I through analyzing intracellular distribution of DOX (Fig. 4F). In the absence of NIR irradiation, DOX fluorescence signals predominantly localized in the cytoplasm, indicating that the DOX molecules remained encapsulated within nanogel. However, Under NIR irradiation, a rapid increase in DOX fluorescence intensity was observed in the nucleus within 1 h postirradiation, indicating the release of DOX from the nanogel due to nanogel disintegration induced by ICG-generated ROS. Considering that free DOX molecules bind to DNA and localize within nucleus, we evaluated the ROS-sensitive DOX release capacity of PCP-NG@D&I through analyzing intracellular distribution of DOX (Fig. 4F). In the absence of NIR irradiation, DOX fluorescence signals predominantly localized in the cytoplasm, indicating that the DOX molecules remained encapsulated within nanogel. However, under NIR irradiation, a rapid increase in DOX fluorescence intensity was observed in the nucleus within 1 h post-irradiation, indicating the release of DOX from the nanogel due to nanogel disintegration induced by ICG-generated ROS.

3.4 ROS-generation and cytotoxicity

Given the critical role of ROS generation in both controlled DOX release and its synergistic antitumor effects, we evaluated the ROS generation capacity of NG@D&I and PCP-NG@D&I nanogels in tumor cells, with and without NIR irradiation (Fig. 4F and G). ROS generation was detected using the probe 2',7'-dichlorofluorescein diacetate (DCFH-DA), which emits green fluorescence upon oxidized by ROS. In the absence of NIR irradiation, no significant ROS-related fluorescence signals were observed. However, under NIR irradiation, substantial ROS fluorescence signals were detected, with the fluorescence intensity in cells treated with PCP-NG@D&I being approximately twice as high as in cells treated with NG@D&I. These findings demonstrate that PCP-NG@D&I nanogels effectively deliver ICG into cells, triggering ROS generation.

We further evaluated the cytotoxicity of different nanogels to tumor cells, with or without NIR irradiation (Fig. 5A). Blank nanogels without DOX and ICG (PCP-NG) exhibited minimal cytotoxicity under NIR irradiation, with cell viability remaining as high as 90%. Treatment with DOX alone (PCP-NG@D) and ICG alone (PCP-NG@I with NIR) resulted in IC50 values of 2.35 μg mL⁻¹ and 19.2 μg mL⁻¹, respectively. Nanogels lacking CDM and CPP peptides (PC-NG@D&I and PP-NG@D&I) yielded IC₅₀ values of 0.7 μg mL⁻¹ and 0.72 μg mL⁻¹, respectively. In contrast, PCP-NG@D&I treatment achieved the lowest IC_{50} value of 0.58 µg mL⁻¹, enhancing tumor cells sensitivity to DOX by 5-fold compared to PCP-NG@D treatment. Next, we evaluated cellular apoptosis induced by different nanogels (Fig. 5B). The percentages of apoptotic tumor cells in the groups treated with DOX and ICG alone were 11.28% and 22.11%, respectively. However, combination treatments with PP-NG@D&I, PC-NG@D&I, and PCP-NG@D&I increased the percentage of apoptotic cells to 42.13%, 35.19%, and 68.81%, respectively. These results demonstrate that co-delivery of ICG significantly enhances tumor cell sensitivity to DOX, leading to a synergistic antitumor effect. Additionally, the exposure of pH-sensitive CPP and ROS-triggered DOX release further strengthened this synergism.

3.5 In vivo biodistribution and antitumor effect of nanogels

Encouraged by the *in vitro* results, we proceeded to evaluate the *in vivo* antitumor effects of different nanogels. We first investigated the tumor enrichment capacity of nanogels with and without CDM structure (Fig. 6A). Six-week-old female nude mice with subcutaneously transplanted MDA-MB-231 tumors were used as animal models. To assess the *in vivo* biodistribution of the nanogels, animals were randomly divided into two groups (PCP-NG@D&I and PC-NG@D&I without the CDM structure) and imaged using an *in vivo* living animal imaging system. Fluorescence signals from ICG increased over

Paper

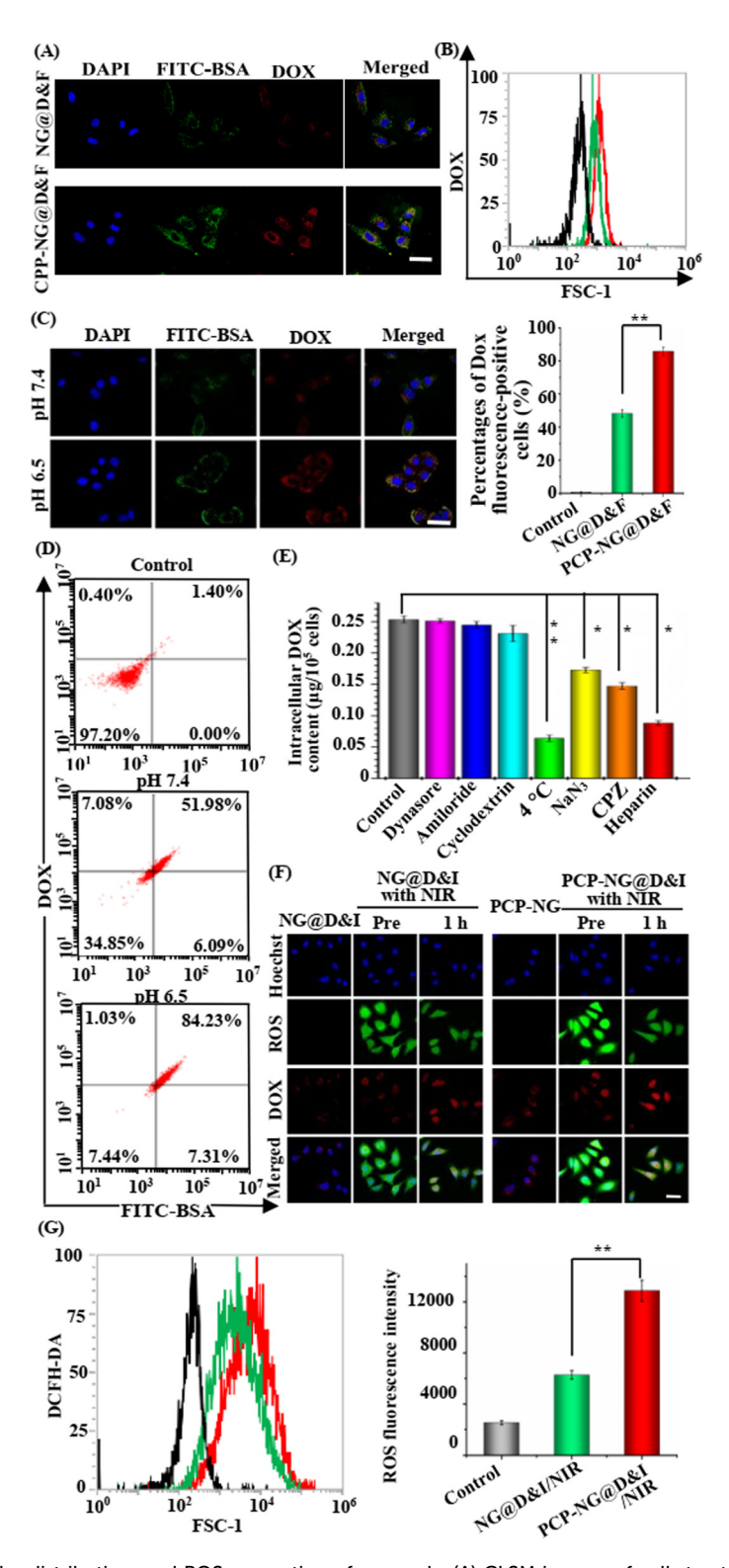


Fig. 4 Cellular uptake, intracellular distribution, and ROS generation of nanogels. (A) CLSM images of cells treated with nanogels, with or without CPP peptide modification. (B) Quantitative analysis of the cellular uptake efficiency of NG@DθF and PCP-NG@DθF nanogels using flow cytometry. Scale bar, 20 μm. (C) CLSM images of cells treated with PCP-NG@DθF at pH 7.4 and pH 6.5. (D) Percentages of DOX- and FITC-positive cells treated with PCP-NG@DθF at pH 7.4 and pH 6.5. (E) Endocytosis pathway analysis of PCP-NG@DθI, determined by intracellular DOX content in the presence of different inhibitors at pH 6.5. (F) CLSM images intracellular distribution of DOX and ROS generation in NG@DθI and PCP-NG@DθI, with or without NIR irradiation. "Pre" refers to the time before treatment. (G) Quantitative analysis of ROS generation capacity of NG@DθI and PCP-NG@DθI with NIR irradiation. BSA proteins were labeled with the green fluorescence dye FITC instead of ICG to monitor cellular uptake and intracellular distribution. Nuclei were stained blue with Hoechst dye, DOX emitted red fluorescence, and ROS were detected with the prober DCFH-DA, which emits green fluorescence. Scale bar, 20 μm. Data are presented as mean \pm SD of three replicates. *p < 0.05 and **p < 0.01.

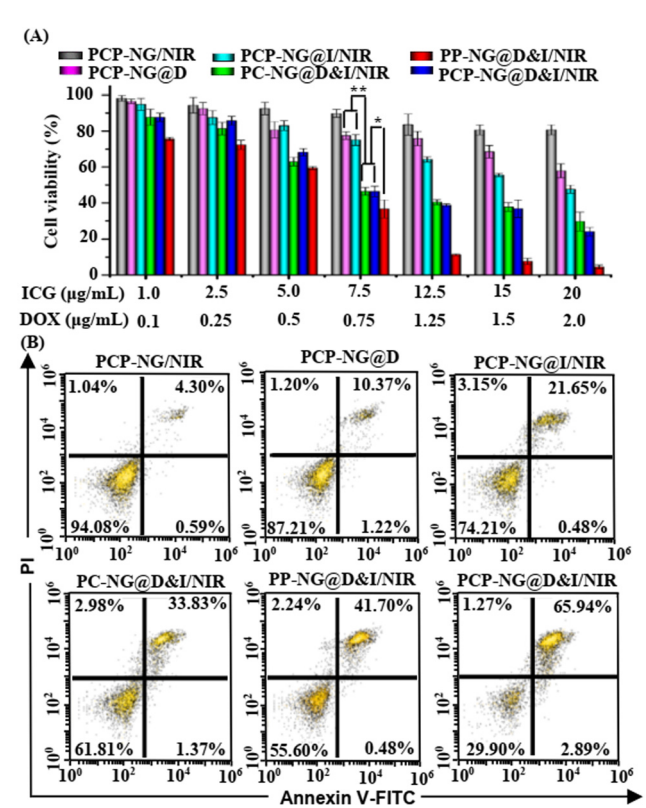


Fig. 5 Cytotoxicity and cellular apoptosis induced by different nanogels. (A) Cytotoxicity of different nanogels to tumor cells, as determined by MTT assay, (B) apoptosis induced by different nanogels, assessed by flow cytometry assay. Data are presented as mean \pm SD of three replicates. *p < 0.05 and **p < 0.01.

time, reaching their maximum at 24 h after nanogel injections in the tumor tissues of both treatment groups (Fig. 6A), indicating that the nanogels had a long circulation time, possibly due to shielding effect of PEG and betaine. Notably, the fluorescence intensity in the tumor tissues was greater for the PCP-NG@D&I nanogels compared to the PC-NG@D&I group, which can be attributed to CPP exposure caused by CDM cleavage and PEG de-shielding. Additionally, fluorescence imaging of major organs excised from animals treated with PCP-NG@D&I showed higher ICG signal intensity in the tumor tissue compared to the PC-NG@D&I group, while fluorescence levels in other organs were similar between the two groups (Fig. 6B). We further assessed the blood circulation time of nanogels with and without the PEG layer (PCP-NG@D&I and CPP-NG@D&I). Compared to the near-complete disappearance of ICG fluorescence signal in animals receiving CPP-NG@D&I, nearly 50% of injected ICG fluorescence remained in the PCP-NG@D&I group (Fig. S9†), confirming the shielding effect of PEG layer. These results reaffirm that PCP-NG@D&I nanogels possess superior tumor tissue enrichment capacity, driven by pH 6.5-triggered PEG de-shielding.

Next, animals bearing tumor cells were randomly divided into eight treatment groups for the *in vivo* antitumor study (Fig. 6C): PBS control, blank nanogel without DOX and ICG

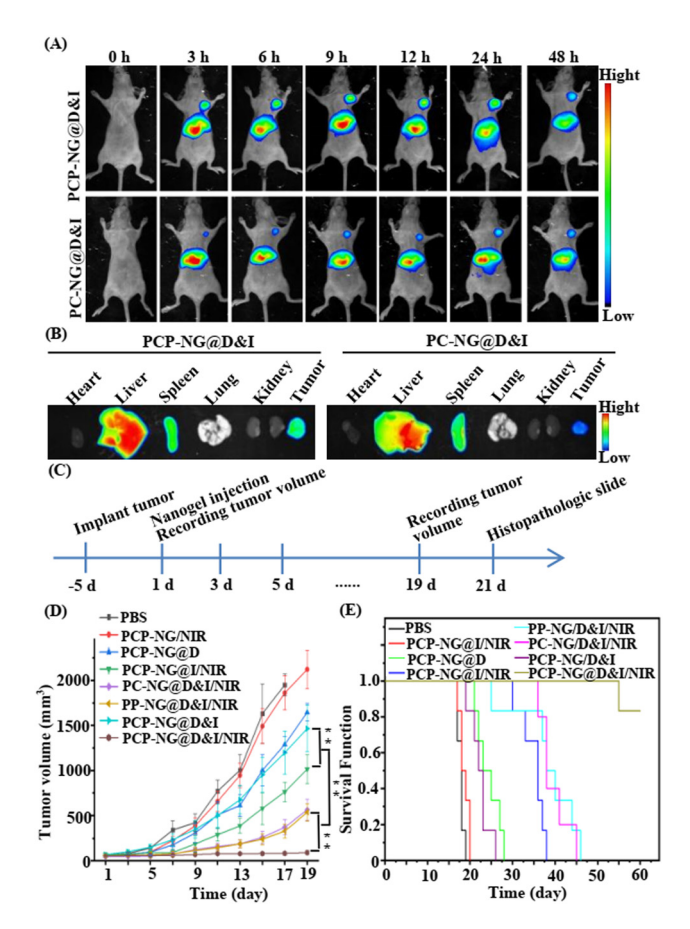


Fig. 6 In vivo biodistribution of nanogels and antitumor efficacy. (A) In vivo fluorescence images of nanogels' distribution. (B) Fluorescence imaging of excised major organs and tumor tissues. (C) Schematic diagram of antitumor therapy regimen. (D) Tumor volumes and (E) survival times of animals treated with different nanogel treatments. Data are presented as mean + SD of three replicates. ** indicates p < 0.01.

(PCP-NG/NIR), DOX alone (PCP-NG@D without irradiation), ICG alone (PCP-NG@I/NIR), pH-nonsensitive combination therapy (PP-NG@D&I/NIR), combination therapy without CPP peptides (PC-NG@D&I/NIR), combination therapy without NIR irradiation (PCP-NG@D&I), and combination therapy with NIR irradiation (PCP-NG@D&I/NIR). Except for the DOX alone (PCP-NG@D) and combination therapy without NIR irradiation (PCP-NG@D&I) treatments, all tumor tissues were irradiated with NIR laser. When tumor volume reached 100 mm³, animals were subjected to different treatments. Without DOX and ICG, both PBS and PCP-NG/NIR treatments did not inhibit tumor growth. DOX and ICG alone treatments (PCP-NG@D and PCP-NG@I/NIR) reduced tumor growth by 22.46% and 52.20% (Fig. 6D), respectively, compared to the PCP-NG/NIR treatment. In contrast, combination treatments (PC-NG@D&I/NIR, PP-NG@D&I/NIR, and PCP-NG@D&I/NIR) reduced tumor growth by 73.45%, 74.78%, and 95.71%, respectively. Notably, PCP-NG@D&I/NIR treatment nearly completely inhibited tumor growth, leaving tumor volumes at just 90.93 mm³. Additionally, without NIR irradiation,

PCP-NG@D&I treatment only reduced tumor growth by 30.96%, which was nearly identical to the effect of PCP-NG@D treatment.

All animals treated with PBS and PCP-NG died within 20 d after the first nanogel injection. The single drug treatments, PCP-NG@D and PCP-NG@I with NIR irradiation, extended survival to 28 d and 38 d (Fig. 6E), respectively. In contrast, 82% of animal treated with PCP-NG@D&I with NIR irradiation survived beyond 60 d. In the absence of NIR irradiation (PCP-NG@D&I treatment), the animals died within 26 d due to the lack of ROS generation, which hindered DOX release. The reduced survival times in the PC-NG@D&I and PP-NG@D&I groups were attributed to the absence or inactivation of CPP peptides. Besides, no significant differences in body weight were observed across different treatment groups (Fig. S10†).

Haematoxylin and eosin stain (H&E) and terminal deoxynucleotidyltransferase-mediated dUTP-biotin nick end labeling (TUNEL) analyses were conducted to further evaluate the synergistic effect of photodynamic-chemotherapy using tumor sections from animals sacrificed at 21 d after first nanogel injection (Fig. 7). In the PBS and blank nanogel groups, typical

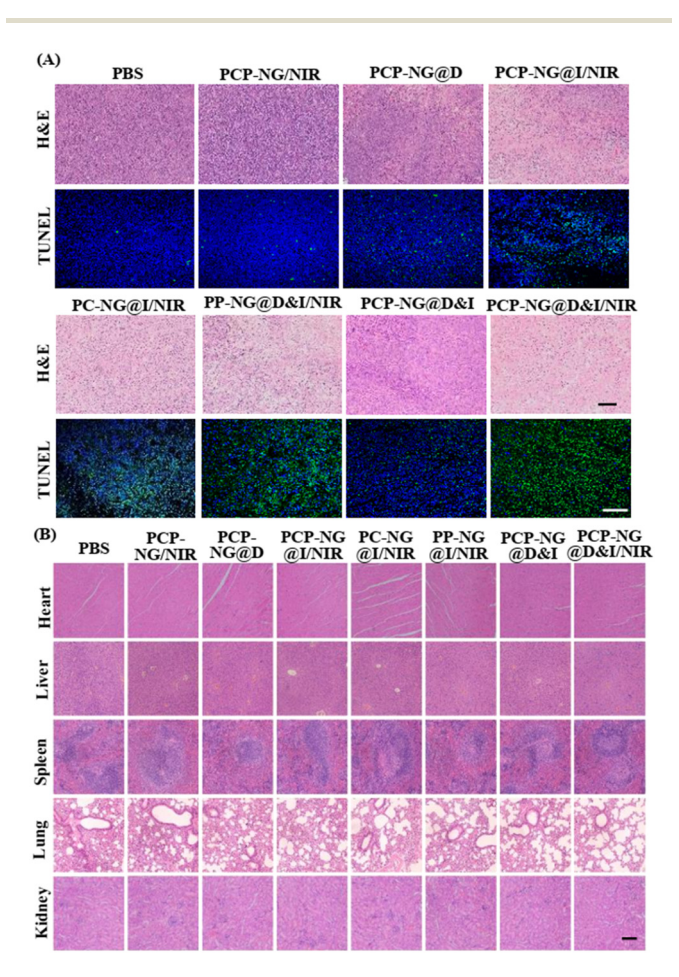


Fig. 7 Histological and immunohistochemical analyses of tumor and major organic tissue sections from animals treated with different nanogels. (A) H&E and TUNEL staining of tumor tissue sections. Black scale bar, 50 μ m; white scale bar, 100 μ m. (B) H&E staining of major organ tissue sections. Scale bar, 250 μ m.

tumor histology was observed, including hypercellularity, pronounced nuclear polymorphism, and hemorrhagic foci (Fig. 7A). In contrast, single-drug treatments (PCP-NG@D and PCP-NG@I) reduced tumor cell density and increased the proportion of apoptotic cells, attributable to the chemotherapeutic effect of released DOX or the ICG-mediated photodynamic effect. Combination treatments induced a greater level of cell death and apoptosis in the tumor tissue sections compared to the single-drug treatments, attributing to the synergistic effect of DOX and ICG. Notably, tumors from animals treated with PCP-NG@D&I under NIR irradiation displayed the fewest viable tumor cells and the highest levels of apoptosis, characterized by chromatin condensation and nuclear fragmentation. These results confirm once again the synergistic antitumor effect of DOX and ICG, achieved through tumor tissue matrix microenvironment-triggered CPP activation and ICG/NIRinduced DOX release, as previously described. Additionally, the major organs of animals treated with different formulations showed nearly normal histological structures (Fig. 7B), indicating that the high biosafety of nanogels. No significant differences were observed in the blood biochemistry indicators between PCP-NG@D&I/NIR and PBS groups (Fig. S11†), suggesting that the PCP-NG@D&I/NIR treatment did not affect liver or kidney function.

4. Conclusions

In this study, we developed a facile co-delivery nanosystem for combination therapy involving photodynamic therapy and chemotherapy. This betaine nanogel-based co-delivery system, prepared *via* inverse miniemulsion polymerization, offers several advantages, including a simple process, easy preparation of monomer and crosslinker, tumor tissue microenvironment-activated cellular uptake, ROS-sensitive drug release. These properties contribute to enhanced tumor cells-specific uptake and spatially controlled drug release. The synergistic effects of the resulting nanogels—activating tumor-specific cellular uptake, controlling drug release, and achieving antitumor outcomes—were validated through a series of *in vitro* and *in vivo* experiments.

Author contributions

D. C., J. Y., and M. Z. conceptualized the study. D. C., J. Y., Q. C., and M. Z. designed the experiments. J. Y., Q. C., Y. J., Q. C., and M. Z. synthesized, imaged, and characterized the nanogel. X. L., D. Y., and S. L. performed biological experiments. D. C., C. O., H. L., and C. H. analyzed the data and wrote the original draft, and D. C. supervised all the work. All authors contributed to the article and approved the submitted version.

Data availability

The authors confirm that the data supporting the findings of this study are available within the article and its ESI.†

Conflicts of interest

There are no conflicts to declare.

Acknowledgements

This work was supported by the National Natural Science Foundation of China (22275215 and 22475244), the International Cooperation Project of Guangdong Provincial Department of Science and Technology (2022A0505050031), and the Natural Science Foundation of Guangdong Province (2022A1515011304).

References

- 1 C. Mamot, R. Ritschard, A. Wicki, G. Stehle, T. Dieterle, L. Bubendorf, C. Hilker, S. Deuster, R. Herrmann and C. Rochlitz, Tolerability, safety, pharmacokinetics, and efficacy of doxorubicin-loaded anti-EGFR immunoliposomes in advanced solid tumours: a phase 1 dose-escalation study, *Lancet Oncol.*, 2012, 13(12), 1234–1241.
- 2 W. Chen, Y. Yuan, D. Cheng, J. Chen and L. Wang, Co-delivery of doxorubicin and siRNA with reduction and pH dually sensitive nanocarrier for synergistic cancer therapy, *Small*, 2014, 10(13), 2678–2687.
- 3 D. Cheng, N. Cao, J. Chen, X. Yu and X. Shuai, Multifunctional nanocarrier mediated co-delivery of doxorubicin and siRNA for synergistic enhancement of glioma apoptosis in rat, *Biomaterials*, 2012, 33(4), 1170–1179.
- 4 L. Zhang, H. Xiao, J. Li, D. Cheng and X. Shuai, Co-delivery of doxorubicin and arsenite with reduction and pH dual-sensitive vesicle for synergistic cancer therapy, *Nanoscale*, 2016, 8(25), 12608–12617.
- 5 H. Xiao, J. He, X. Li, B. Li, L. Zhang, Y. Wang, D. Cheng and X. Shuai, Polymeric nanovesicles as simultaneous delivery platforms with doxorubicin conjugation and elacridar encapsulation for enhanced treatment of multidrugresistant breast cancer, *J. Mater. Chem. B*, 2018, **6**(45), 7521–7529.
- 6 C. Du, D. Deng, L. Shan, S. Wan, J. Cao, J. Tian, S. Achilefu and Y. Gu, A pH-sensitive doxorubicin prodrug based on folate-conjugated BSA for tumor-targeted drug delivery, *Biomaterials*, 2013, 34(12), 3087–3097.
- 7 X. Liu, C. Wang, H. Ma, F. Yu, F. Hu and H. Yuan, Water-responsive hybrid nanoparticles codelivering ICG and DOX effectively treat breast cancer via hyperthermia-aided DOX functionality and drug penetration, *Adv. Healthcare Mater.*, 2019, 8(8), 1801486.

- 8 J. Zhou, J. Gu, X. Sun, Q. Ye, X. Wu, J. Xi, J. Han and Y. Liu, Supramolecular chiral binding affinity-achieved efficient synergistic cancer therapy, *Adv. Sci.*, 2024, **11**(16), 2308493.
- 9 L. Wu, M. Jiang, C. Chu, T. Luo, Y. Hui, W. Zhou, S. Geng and X.-F. Yu, Transformation of black phosphorus through lattice reconstruction for NIR-II-responsive cancer therapy, *Adv. Sci.*, 2024, **11**(3), 2305762.
- 10 G. Zhou, H. Xiao, X. Li, Y. Huang, W. Song, L. Song, M. Chen, D. Cheng and X. Shuai, Gold nanocage decorated pH-sensitive micelle for highly effective photothermochemotherapy and photoacoustic imaging, *Acta Biomater.*, 2017, 64, 223–236.
- 11 L. Wang, Y. Yuan, S. Lin, J. Huang, J. Dai, Q. Jiang, D. Cheng and X. Shuai, Photothermo-chemotherapy of cancer employing drug leakage-free gold nanoshells, *Biomaterials*, 2016, 78, 40–49.
- 12 F. Wang, Y. Wang, S. Dou, M. Xiong, T. Sun and J. Wang, Doxorubicin-tethered responsive gold nanoparticles facilitate intracellular drug delivery for overcoming multidrug resistance in cancer cells, ACS Nano, 2011, 5(5), 3679–3692.
- 13 S. Ruan, M. Yuan, L. Zhang, G. Hu, J. Chen, X. Cun, Q. Zhang, Y. Yang, Q. He and H. Gao, Tumor microenvironment sensitive doxorubicin delivery and release to glioma using angiopep-2 decorated gold nanoparticles, *Biomaterials*, 2015, 37, 425–435.
- 14 X. Liu, J. Du, Z. Xie, L. Wang, X. Liu, Z. Hou, X. Wang and R. Tang, Lactobionic acid-modified phycocyanin nanoparticles loaded with doxorubicin for synergistic chemophotodynamic therapy, *Int. J. Biol. Macromol.*, 2021, 186, 206–217.
- 15 Q. Ren, Z. Liang, X. Jiang, P. Gong, L. Zhou, Z. Sun, J. Xiang, Z. Xu, X. Peng, S. Li, W. Li, L. Cai and J. Tang, Enzyme and pH dual-responsive hyaluronic acid nanoparticles mediated combination of photodynamic therapy and chemotherapy, *Int. J. Biol. Macromol.*, 2019, 130, 845–852.
- 16 S. Yan, P. Sun, N. Niu, Z. Zhang, W. Xu, S. Zhao, L. Wang, D. Wang and B. Tang, "One stone, four birds" ion engineering to fabricate versatile core–shell organosilica nanoparticles for intelligent nanotheranostics, ACS Nano, 2022, 16(6), 9785–9798.
- 17 L. Luo, Y. Qi, H. Zhong, S. Jiang, H. Zhang, H. Cai, Y. Wu, Z. Gu, Q. Gong and K. Luo, GSH-sensitive polymeric prodrug: synthesis and loading with photosensitizers as nanoscale chemo-photodynamic anti-cancer nanomedicine, *Acta Pharm. Sin. B*, 2022, 12(1), 424–436.
- 18 Y. Zhang, M. Zhang, X. Hu, H. Hao, C. Quan, T. Ren, H. Gao and J. Wang, Engineering a porphyrin COFs encapsulated by hyaluronic acid tumor-targeted nanoplatform for sequential chemo-photodynamic multimodal tumor therapy, *Int. J. Biol. Macromol.*, 2024, 279, 135328.
- 19 D. Tang, Y. Yu, J. Zhang, X. Dong, C. Liu and H. Xiao, Self-sacrificially degradable pseudo-semiconducting polymer nanoparticles that integrate NIR-II fluorescence bioimaging, photodynamic immunotherapy, and photo-activated chemotherapy, Adv. Mater., 2022, 34(34), 2203820.

Paper

20 B. Yu, M. Liu, L. Jiang, C. Xu, H. Hu, T. Huang, D. Xu, N. Wang, Q. Li, B. Z. Tang, X. Huang and W. Zhang, Aggregation-induced emission photosensitizer-engineered anticancer nanomedicine for synergistic chemo/chemodynamic/photodynamic therapy, *Adv. Healthcare Mater.*, 2024, 13(11), 2303643.

- 21 S. Deng, S. Wang, Z. Xiao and D. Cheng, Unprotonatable and ROS-sensitive nanocarrier for NIR spatially activated siRNA therapy with synergistic drug effect, *Small*, 2022, 18(41), 2203823.
- 22 D. Guo, X. Ji, F. Peng, Y. Zhong, B. Chu, Y. Su and Y. He, Photostable and biocompatible fluorescent silicon nanoparticles for imaging-guided co-delivery of siRNA and doxorubicin to drug-resistant cancer cells, *Nano-Micro Lett.*, 2019, **11**(1), 27.
- 23 K. Butowska, X. Han, N. Gong, R. El-Mayta, R. M. Haley, L. Xue, W. Zhong, W. Guo, K. Wang and M. J. Mitchell, Doxorubicin-conjugated siRNA lipid nanoparticles for combination cancer therapy, *Acta Pharm. Sin. B*, 2023, 13(4), 1429–1437.
- 24 C. Xu, D. Li, Z. Cao, M. Xiong, X. Yang and J. Wang, Facile hydrophobization of siRNA with anticancer drug for noncationic nanocarrier-mediated systemic delivery, *Nano Lett.*, 2019, 19(4), 2688–2693.
- 25 M. Kim, J. S. Lee, W. Kim, J. H. Lee, B.-H. Jun, K.-S. Kim and D.-E. Kim, Aptamer-conjugated nano-liposome for immunogenic chemotherapy with reversal of immunosuppression, *J. Controlled Release*, 2022, 348, 893–910.
- 26 A. M. S. Khesht, V. Karpisheh, P. S. Gilan, L. A. Melnikova, A. O. Zekiy, M. Mohammadi, M. Hojjat-Farsangi, N. M. Zolbanin, A. Mahmoodpoor, H. Hassannia, L. Aghebati-Maleki, R. Jafari and F. Jadidi-Niaragh, Blockade of CD73 using siRNA loaded chitosan lactate nanoparticles functionalized with TAT-hyaluronate enhances doxorubicin mediated cytotoxicity in cancer cells both in vitro and in vivo, *Int. J. Biol. Macromol.*, 2021, 186, 849–863.
- 27 H.M. Abdel-Bar, A.A. Walters, Y. Lim, N. Rouatbi, Y. Qin, F. Gheidari, S. Han, R. Osman, J.T. W. Wang and K.T. Al-Jamal, An "eat me" combinatory nano-formulation for systemic immunotherapy of solid tumors, *Theranostics*, 2021, 11(18), 8738–8754.
- 28 P. Kumar, R. Salve, K. M. Paknikar and V. Gajbhiye, Nucleolin aptamer conjugated MSNPs-PLR-PEG multifunctional nanoconstructs for targeted co-delivery of anticancer drug and siRNA to counter drug resistance in TNBC, *Int. J. Biol. Macromol.*, 2023, 229, 600–614.
- 29 Q. Duan, Y. Zhu, H. Jia, Y. Guo, X. Zhang, R. Gu, C. Li and F. Wu, Platinum-coordinated dual-responsive nanogels for universal drug delivery and combination cancer therapy, *Small*, 2022, 18(46), 2203260.
- 30 Y. Zhao, X. Cheng, J. Li, S. Liu, J. Meng, W. Li, C. Yang, Y. Wen, S. Mi, H. Huo, H. Xu and X. Lu, Pulmonary delivery of immune checkpoint inhibitors using a responsive polyethylene glycol nanogel for treating lung metastasis, *Nano Today*, 2023, **52**, 101988.

- 31 X. Zeng, M. Zuo, J. Yuan, G. Chen, S. Liu, C. Ou, Q. Chen, C. Wei, D. Yu and D. Cheng, Electrostatic interactions-independent approach for efficient siRNA encapsulation with stimuli-responsive charge reversal and controlled release, *Adv. Funct. Mater.*, 2025, 35(1), 2406122.
- 32 Y. Hu, S. Gao, H. Lu, S. Tan, F. Chen, Y. Ke and J. Y. Ying, A self-immolative DNA nanogel vaccine toward cancer immunotherapy, *Nano Lett.*, 2023, 23(21), 9778–9787.
- 33 M. Ghomi, E. N. Zare, H. Alidadi, N. Pourreza, A. Sheini, N. Rabiee, V. Mattoli, X. Chen and P. Makvandi, A multifunctional bioresponsive and fluorescent active nanogel composite for breast cancer therapy and bioimaging, *Adv. Compos. Hybrid Mater.*, 2023, 6(1), 51.
- 34 W. He, D. Qian, Y. Wang, G. Zhang, Y. Cheng, X. Hu, K. Wen, M. Wang, Z. Liu, X. Zhou and M. Zhu, A protein-like nanogel for spinning hierarchically structured artificial spider silk, *Adv. Mater.*, 2022, 34(27), 2201843.
- 35 Z. Zhou, K. Li, Y. Guo, P. Liu, Q. Chen, H. Fan, T. Sun and C. Jiang, ROS/electro dual-reactive nanogel for targeting epileptic foci to remodel aberrant circuits and inflammatory microenvironment, *ACS Nano*, 2023, **17**(8), 7847–7864.
- 36 H.-Y. Mu, Y.-N. N. Ta, M. J. R. Tham, F.-F. Hsu, Y.-C. Lin, H.-C. Huang, Y.-C. Sung, C.-I. Huang, C.-L. Wu, C.-H. Chang, S. Yang, T.-Y. Lee, D. Wan, J. Wang, D. G. Duda, Y. Boucher, J.-H. Huang, W. H. Ang and Y. Chen, A Chemoimmunotherapy nanogel enables efficient delivery of interleukin-2 and induction of immunogenic cell death for effective cancer therapy, Adv. Funct. Mater., 2024, 34(1), 2303033.
- 37 H. F. Mathews, M. I. Pieper, S.-H. Jung and A. Pich, Compartmentalized polyampholyte microgels by depletion flocculation and coacervation of nanogels in emulsion droplets, *Angew. Chem., Int. Ed.*, 2023, **62**(36), e202304908.
- 38 F. Zhang, J. Dong, K. Huang, B. Duan, C. Li, R. Yang, J. Li, F. Zhi, Z. Zhou and M. Sun, "Dominolike" barriers elimination with an intratumoral adenosine-triphosphate-supersensitive nanogel to enhance cancer chemoimmunotherapy, *ACS Nano*, 2023, 17(19), 18805–18817.
- 39 B. Li, Z. Yuan, Y. He, H. Hung and S. Jiang, Zwitterionic nanoconjugate enables safe and efficient lymphatic drug delivery, *Nano Lett.*, 2020, **20**(6), 4693–4699.
- 40 A. Sinclair, M. B. O'Kelly, T. Bai, H. C. Hung, P. Jain and S. Jiang, Self-healing zwitterionic microgels as a versatile platform for malleable cell constructs and injectable therapies, *Adv. Mater.*, 2018, 30(39), 1803087.
- 41 Q. Li, C. Wen, J. Yang, X. Zhou, Y. Zhu, J. Zheng, G. Cheng, J. Bai, T. Xu, J. Ji, S. Jiang, L. Zhang and P. Zhang, Zwitterionic biomaterials, *Chem. Rev.*, 2022, 122(23), 17073–17154.
- 42 Q. Wang, M. Li, T. Cui, R. Wu, F. Guo, M. Fu, Y. Zhu, C. Yang, B. Chen and G. Sun, A novel zwitterionic hydrogel incorporated with graphene oxide for bone tissue engineering: synthesis, characterization, and promotion of osteogenic differentiation of bone mesenchymal stem cells, *Int. J. Mol. Sci.*, 2023, 24(3), 2691.

43 T. Jeon, R. Goswami, H. Nagaraj, Y. A. Cicek, V. Lehot, J. Welton, C. J. Bell, J. Park, D. C. Luther, J. Im, C. M. Rotello, J. Mager and V. M. Rotello, Engineered zwitterionic diblock copolymer–siRNA polyplexes provide highly effective treatment of triple–negative breast cancer in a 4 T1 murine model, *Adv. Funct. Mater.*, 2024, 34(42), 2406763.

Biomaterials Science

- 44 S. Deng, X. Li, S. Liu, J. Chen, M. Li, S. Y. Chew, K. W. Leong and D. Cheng, Codelivery of CRISPR-Cas9 and chlorin e6 for spatially controlled tumor-specific gene editing with synergistic drug effects, *Sci. Adv.*, 2020, **6**(29), eabb4005.
- 45 Z. Su, Z. Xiao, Y. Wang, J. Huang, Y. An, X. Wang and X. Shuai, Codelivery of anti-PD-1 antibody and paclitaxel with matrix metalloproteinase and pH dual-sensitive micelles for enhanced tumor chemoimmunotherapy, *Small*, 2020, **16**(7), 1906832.
- 46 Y. Zhang, S. Li, P. Jin, T. Shang, R. Sun, L. Lu, K. Guo, J. Liu, Y. Tong, J. Wang, S. Liu, C. Wang, Y. Kang, W. Zhu, Q. Wang, X. Zhang, F. Yin, Y. E. Sun and L. Cui, Dual functions of microRNA-17 in maintaining cartilage homeostasis and protection against osteoarthritis, *Nat. Commun.*, 2022, 13(1), 2447.
- 47 T. Sun and C. Jiang, Stimuli-responsive drug delivery systems triggered by intracellular or subcellular microenvironments, *Adv. Drug Delivery Rev.*, 2023, **196**, 114773.

- 48 S. Wang, G. Yu, Z. Wang, O. Jacobson, L. S. Lin, W. Yang, H. Deng, Z. He, Y. T. Liu, Z. Y. Chen and X. Chen, Enhanced antitumor efficacy by a cascade of reactive oxygen species generation and drug release, *Angew. Chem.*, 2019, 131(41), 14900–14905.
- 49 C. Yao, W. Wang, P. Wang, M. Zhao, X. Li and F. Zhang, Near-infrared upconversion mesoporous cerium oxide hollow biophotocatalyst for concurrent pH-/H₂O₂-responsive O₂ evolving synergetic cancer therapy, *Adv. Mater.*, 2018, 30(7), 1704833.
- 50 Y. Yang, W. Zeng, P. Huang, X. Zeng and L. Mei, Smart materials for drug delivery and cancer therapy, *VIEW*, 2021, 2(2), 20200042.
- 51 G. Chen, S. Deng, S. Liu, Y. Zhao, Y. Xiao, X. Zeng, Y. Xu, D. Cheng and B. Chen, pH and ROS dual-sensitive nanocarriers for the targeted co-delivery and on-demand sequential release of tofacitinib and glucosamine for synergistic rheumatoid arthritis treatment, *Small*, 2024, 20(24), 2308520.
- 52 C. Li, P. Wu, Y. Dou, Q. Li and J. Zhang, Bioresponsive nanoplatforms for imaging and therapy of cardiovascular diseases, *VIEW*, 2022, 3(1), 20200137.
- 53 R. S. Gamage and B. D. Smith, Fluorescence imaging using deep-red indocyanine blue, a complementary partner for near-infrared indocyanine green, *Chem. Biomed. Imaging*, 2024, 2(5), 384–397.